Engineering Fracture Mechanics 259 (2022) 108126

Contents lists available at ScienceDirect

Engineering Fracture Mechanics

journal homepage: www.elsevier.com/locate/engfracmech

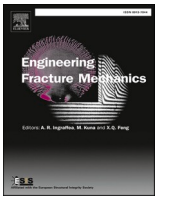

A strain-rate cohesive fracture model of rocks based on Lennard-Jones potential

Qindong Lin [a], Shihai Li [b,c], Yundan Gan [a], Chun Feng [b,*]

[a] Xi'an Modern Chemistry Research Institute, Xi'an, Shaanxi 710065, China
[b] Key Laboratory for Mechanics in Fluid Solid Coupling Systems, Institute of Mechanics, Chinese Academy of Sciences, Beijing 100190, China
[c] School of Engineering Science, University of Chinese Academy of Sciences, Beijing 100049, China

ARTICLE INFO

Keywords:
Strain-rate effect
Cohesive fracture model
Lennard-Jones potential
CDEM

ABSTRACT

To characterize the dynamic mechanical response of rocks during the initiation and propagation of cracks at a high strain rate, a strain-rate cohesive fracture model is established based on the Lennard-Jones potential and multi-scale model of rocks. The newly proposed model explains the micro-mechanism of strain rate effect from the molecular scale and establishes the potential energy function and force function. First, it is proposed that the strain rate effect arises due to the change of microscopic properties of molecules at a high strain rate. Thereafter, the potential energy function and force function of the strain-rate cohesive fracture model corresponding to the dynamic tensile and shear processes are established. Finally, the accuracy of the strain-rate cohesive fracture model is verified through numerical simulations. The results indicate that the strain-rate cohesive fracture model can accurately simulate the dynamic tensile failure and shear failure of rocks at different strain rates. The dynamic tensile strength, dynamic compressive strength, and dynamic tensile fracture energy obtained by numerical simulations and laboratory tests are similar.

1. Introduction

Rocks can be regarded as aggregates composed of a large number of mineral particles and cementing substances under long-term geological action. Given the wide range of applications of rocks in slope engineering, mining engineering and tunneling, scholars have conducted extensive research on the mechanical properties of rocks [1–8]. The current commonly used laboratory tests of rocks include the uniaxial compression test, triaxial compression test, direct shear test, Brazilian splitting test, semi-circular bend test, etc. [9–14]. Due to the diversity of constituent materials and the complexity of microstructure, the experimental results indicate that rocks have complex mechanical behavior [15–18].

Most of the above-mentioned laboratory tests are static or quasi-static tests. As the fields of blasting, high-velocity impact, earthquake, and rockburst all involve the dynamic properties of rocks, researchers have begun to study the deformation and failure mechanisms of rocks at a high strain rate [19–21]. Since the split Hopkinson pressure bar (SHPB) can realize the impact loading of large-size specimens of heterogeneous materials (e.g., rock, concrete) in the laboratory test, it has become an ideal experimental setup for studying dynamic constitutive relation and dynamic mechanical properties of materials at a high strain rate. Ai [22] explored the crack propagation law and dynamic mechanical properties of rocks under high strain rate impact loading, and concluded that crack

* Corresponding author.
E-mail address: fengchun@imech.ac.cn (C. Feng).

https://doi.org/10.1016/j.engfracmech.2021.108126
Received 4 September 2021; Received in revised form 5 November 2021; Accepted 13 November 2021
Available online 19 November 2021

Nomenclature

G_{fI}	tensile fracture energy
G_{fII}	shear fracture energy
σ_t	tensile strength
ε_0	depth of the L-J potential well
r_0	distance at which the L-J potential is zero
β	thickness ratio
ω	space occupancy ratio
λ	contact ratio
F_L	external load
k_ε	microscopic well depth increasing factor
ε_{st}	value of ε_0 under static loading
ε_{dy}	value of ε_0 under dynamic loading
k_r	microscopic distance increasing factor
r_{st}	value of r_0 under static loading
r_{dy}	value of r_0 under dynamic loading
r_s	distance at which F_{vd} reaches the maximum
r_e	distance at which the L-J potential reaches the minimum
r_d	distance at which van der Waals force is zero
r_{min}	minimum distance between molecules at the initial moment
r_{max}	maximum distance between molecules at the initial moment
Δr_v	increase in the normal distance
N_f^t	number of molecules between adjacent layers during tensile process
r_{dye}	distance at which the L-J potential reaches the minimum under dynamic loading
W_t	potential energy of the entire rupture field during dynamic tensile process
F_t	force of the entire rupture field during dynamic tensile process
F_{maxt}^{dy}	maximum value of tensile force F_t during dynamic tensile process
F_{maxt}^{st}	maximum value of tensile force F_t during static tensile process
G_t^{dy}	tensile fracture energy during dynamic tensile process
G_t^{st}	tensile fracture energy during static tensile process
w_{lj}	Lennard-Jones (L-J) potential
F_{vd}	van der Waals force
N_f^s	number of molecules between adjacent layers during shear process
Δr_u	increase in the tangential distance
W_s	potential energy of the entire rupture field during dynamic shear process
F_s	force of the entire rupture field during dynamic shear process
r_{dy}	distance between two molecules under dynamic loading
F_{maxs}^{dy}	maximum value of shear force F_s during dynamic shear process
F_{maxs}^{st}	maximum value of shear force F_s during static shear process
G_s^{dy}	shear fracture energy during dynamic shear process
G_s^{st}	shear fracture energy during static shear process
ε_i	incident wave
ε_r	reflected wave
ε_t	transmission wave

propagation rate of the crack along X-Y direction both rises with the impact velocity increase. Kong [23] investigated the dynamic characteristics and fracture mechanisms of gas-bearing coal specimen, and found that with the increase of confining pressure and impact load, the dynamic strength and failure strain increased. Fakhimi [24] studied the strength characteristics of sandstone under uniaxial compressive loading, and the results indicated that rock strength increases under dynamic loading. Gong [25] investigated the effects of low confining pressures and high strain rates on the dynamic mechanical properties of sandstone, and proposed that the dynamic uniaxial and triaxial compressive strengths will linearly increase with the logarithm of the strain rate. Zwiessler [26] explored the deformation of rocks in the high strain rate regime experimentally, and found that the onset of dynamic behavior is accompanied with changes in the fracture pattern from single to multiple fractures. Wen [27] evaluated the dynamic properties of a layered composite rock mass, and concluded that increasing strain rate will cause the increases of peak strength and the corresponding failure strain. It can be concluded that the experiment results indicate that the deformation characteristics, failure strength, and fracture toughness of rocks at high strain rates are obviously rate-dependent.

With the development of computer technology and numerical simulation methods (e.g., discrete element method, extended finite

element method, material point method, smoothed particle hydrodynamics, cracking element method, cracking particle method, micropolar peridynamic, coupled algorithm), many researchers began to study the failure process of rocks based on numerical simulation [28–51]. The deformation and failure of rocks are the processes of the initiation, propagation, connection, penetration, and slip of internal microcracks. The generation of fracture planes in rocks requires energy absorption, while the slip between fracture planes requires energy consumption. To accurately characterize the mechanical response characteristics and energy evolution characteristics of rocks during the process of crack initiation and propagation, scholars have proposed a variety of numerical models. Owing to the advantages of clear mechanical meaning and convenience of implementation, the cohesive zone model is widely used to study the fracture process of rock and concrete. Pan [52] proposed a statistical grain-based discrete element method coupling with the cohesive zone model, and studied the strength characteristics, deformation response, and failure mode of rocks. To simulate the damage evolution and fracture process in quasi-brittle materials, Wei [53] developed a modified cohesive damage-plasticity model and verified the correctness and feasibility of the proposed model. Nairn [54] established a strength cohesive zone model, which provides improved modeling for problems with changing mode mixity. Jiang [55] developed a 3D numerical model by inserting cohesive elements into finite elements, and evaluated the rock fracture, penetration force, and chip shape during rock breaking with a conical pick. Taleghani [56] incorporated triaxiality effects into the cohesive zone model, and conducted the sensitivity analysis of primary parameters (e.g., fluid viscosity, natural fracture distribution, fracture intersection angle).

Currently, the cohesive zone model mainly focuses on the fracture process of brittle materials (e.g., rocks, concrete) under static loading. Since it cannot consider the effect of strain rate on mechanical properties, some scholars have begun to add terms that reflect the strain rate effect in the constitutive model. Meng [57] proposed a new bilinear cohesive law that can handle the effects of strain effect and plastic strain, and the tapered double cantilever beam (TDCB) and mixed mode bending (MMB) analyses are used to verify the proposed law. By introducing a rate-dependent cohesive element model into the mesoscale framework, Zhou [58] investigated the dynamic tensile behavior of concrete under high strain rate. Zhao [59] presented a generalized rate-dependent cohesive zone model for describing the interfacial viscoelasticity and progressive damage of mode I fracture, which extended the traditional bi-linear cohesive traction-separation law. Wang [60] proposed a rate-dependent constitutive law for cohesive element model to predict the direction and branching of dynamic crack, and concluded that the fracture process zone of dynamic crack shows a fan shape, of which the radius is also rate-dependent.

Although some scholars have introduced terms reflecting the strain rate effect into the cohesive zone model to describe the dynamic fracture behavior of materials at a high strain rate, the current research on the strain-rate cohesive zone model still has two main limitations. First, the strain-rate cohesive zone model currently studied is mostly based on the bilinear cohesive law. Second, regarding the mechanism of strain rate effect on mechanical properties, few scholars have studied when establishing strain-rate cohesive zone model.

Based on the Lennard-Jones potential between non-bonding molecules and the multi-scale model of rocks, this study first explores the causes of the strain rate effect. Subsequently, a new strain-rate cohesive fracture model is established to accurately characterize the dynamic mechanical response and fracture energy of brittle materials during crack initiation and propagation at a high strain rate.

2. Methodology

In this section, the micro-mechanism of strain rate effect of mechanical properties is first studied, followed by two microscopic dynamic increasing factors are proposed. Finally, based on the multi-scale model of rocks, the Lennard-Jones potential and the microscopic dynamic increasing factors, the functions of potential energy and force during the dynamic tensile process and shear process are established.

2.1. Basic concept

Some deformation energy is dissipated during the process of crack initiation and propagation in brittle materials, and the energy dissipated with crack propagation is defined as fracture energy. In order to more accurately describe the initiation and propagation of cracks and the fracture energy in numerical simulation, scholars have proposed a number of cohesive fracture models. Based on the

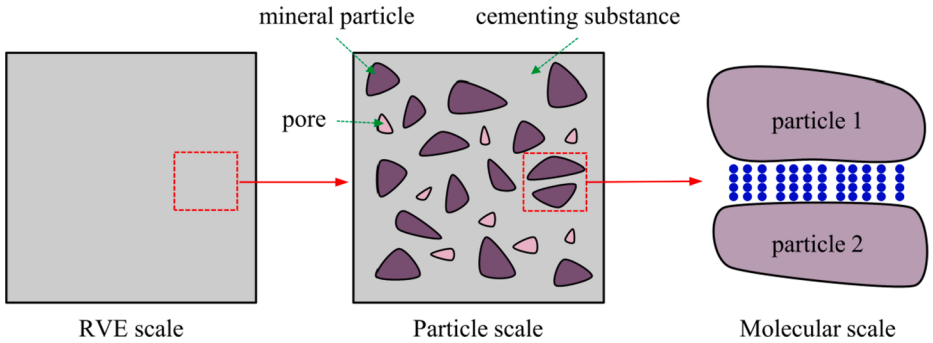

Fig. 1. Schematic diagram of the multi-scale model.

multi-scale model of rocks and the Lennard-Jones potential between non-bonding molecules, Lin [61] proposed a new cohesive fracture model. This model explains the causes of fracture energy during crack initiation and propagation from a microscopic perspective and establishes the correspondence between the macroscopic parameters (fracture energy G_I/G_{II}, tensile strength σ_t) and the microscopic parameters (ε_0, r_0).

To establish the cohesive fracture model, based on the structural and fracture characteristics of rocks, Lin first proposed the multi-scale model of rocks, as shown in Fig. 1. The multi-scale model includes RVE scale, particle scale and molecular scale, and each scale describes the different characteristics of rocks. RVE scale is the basic scale for characterizing the complex structural characteristics and mechanical characteristics of rocks. However, the energy dissipation mechanism and the initiation and propagation process of cracks cannot be studied at this scale. Particle scale is the basic scale for describing the initiation and propagation process of cracks. However, the energy dissipation mechanism cannot be studied at this scale. Molecular scale is the basic scale for studying the energy dissipation mechanism. It is assumed that the cementing substance is composed of a large number of non-bonding molecules, and the Lennard-Jones potential is used to describe the potential energy between non-bonding molecules.

Subsequently, in order to investigate the change law of potential energy and force of the rupture field in the initiation and propagation process of cracks, some key parameters are proposed, including thickness ratio β, space occupancy rate ω and contact ratio λ.

Finally, based on the multi-scale model, Lennard-Jones potential and key parameters, the force and potential energy functions of the cohesive fracture model during the tensile process and shear process are established, and the force–displacement curve is plotted in Fig. 2. Fig. 2(a) plots the force–displacement curve in the tensile process, and the green area under the changing curve denotes tensile fracture energy G_{fI}. Fig. 2(b) plots the force–displacement curve in the shear process, and the red area under the changing curve denotes shear fracture energy G_{fII}.

In the cohesive fracture model established by Lin, it is proposed that the essence of fracture energy is the transformation of the deformation energy of the continuous field into the potential energy between the non-bonding molecules in the rupture field.

Compared with other traditional cohesive zone models (e.g., bilinear, linear-parabolic, exponential, trapezoidal), the new cohesive fracture model explains the generative mechanisms of fracture energy from the molecular scale, and makes the variation law of force accompanied by displacement during crack initiation and propagation more well-founded. However, the cohesive fracture model does not explain the effect mechanism of high strain rate on the peak strength and fracture energy.

2.2. Micro-mechanism of strain rate effect

In the cohesive fracture model obtained based on the multi-scale model and Lennard-Jones potential, there are two key parameters, the potential energy well depth ε_0 and the distance r_0 at which the intermolecular potential is zero. These two parameters determine the macroscopic mechanical properties of rocks (e.g., tensile strength σ_t, tensile fracture energy G_I, shear fracture energy G_{II}). For the same class of rocks, the microscopic parameters (ε_0 and r_0) of neutral molecules under static loading are the same if the type of neutral molecules at the molecular scale is the same. Because the arrangement of neutral molecules at the molecular scale is also the same, it means that such rocks have the same macroscopic mechanical properties under static loading. However, current research results show that both temperature and velocity will affect the microscopic parameters of non-bonding molecules.

Nasehzadeh [62] conducted research on the influence of temperature on the microscopic parameters of Lennard-Jones potential energy function. By conducting research on the research objects at different temperatures, Nasehzadeh proposed that the obtained values of Lennard–Jones pair potential parameters are not constant and are dependent on temperature. Dedkov [63,64] conducted research on the influence of velocity on the microscopic parameters of Lennard-Jones potential energy function. The results indicated that the van der Waals atom–surface interaction energy manifests strong nonlinear dependence on the velocity and distance.

Based on the current research results of related scholars, a hypothesis is proposed. In the multi-scale model of rocks, the high strain rate of materials at the RVE scale will lead to changes in microscopic parameters (ε_0 and r_0) at the molecular scale.

For the same neutral molecules in the same type of rocks, since their microscopic parameters (ε_0 and r_0) are the same under static

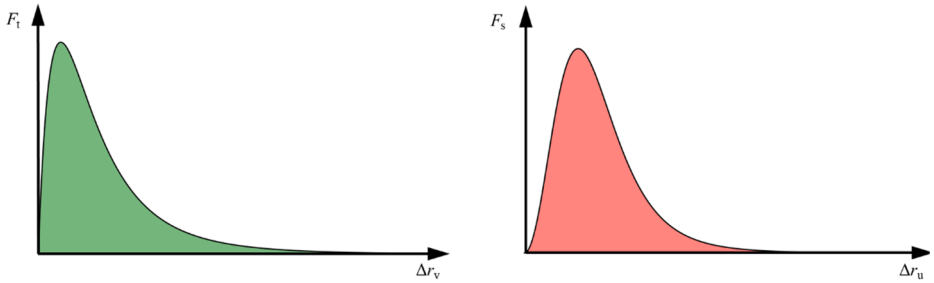

Fig. 2. Force-displacement curve during the tensile and shear process.

loading, and the arrangement of molecules is the same, such rocks have the same macroscopic mechanical properties under static loading. However, as the loading rate of the external load F_L increases, the strain rate at RVE scale increases significantly, leading to an increase in the deformation rate of the cementing substance between mineral particles. For the molecular scale, it means that the separation rate between non-bonding molecules increases significantly, and this leads to changes in the microscopic parameters of non-bonding molecules. Although the arrangement characteristics of molecules at molecular scale do not change, it still causes changes in the macroscopic mechanical properties of rocks, and thus the strain rate effect on macroscopic mechanical properties appears.

Based on the above theoretical analysis, an important conclusion is drawn. The essence of the strain rate effect on the macroscopic mechanical properties is that high strain rate leads to changes in the microscopic mechanical parameters between non-bonding molecules, which in turn leads to changes in the macroscopic mechanical properties of materials at different strain rates.

Given that there are two key parameters in the Lennard-Jones potential, and different molecular microscopic parameters are not equally sensitive to high strain rates. Thus the effect of high strain rate at RVE scale on molecular microscopic parameters is divided into three cases, which only affect ε_0, only affect r_0, and affect both ε_0 and r_0.

Next, the variation characteristics of the macroscopic mechanical properties will be obtained by studying the microscopic parameters between non-bonding molecules.

2.3. Key parameters

The current research results have indicated that the velocity affects the microscopic parameters of non-bonding molecules, but there are no clear and simplified functions to characterize the change law of ε_0 and r_0 in the Lennard-jones potential at different velocities. Based on the hypothesis presented in Section 2.2, two key microscopic parameters are proposed to quantify the effect of high strain rates at RVE scale on the microscopic mechanical parameters of molecules.

2.3.1. Microscopic well depth increasing factor k_ε

In the basic hypothesis of Section 2.2, it is assumed that the high strain rate at RVE scale will lead to changes in the microscopic mechanical parameters between non-bonding molecules. In order to quantify the effect of high strain rate on the microscopic mechanical parameters ε_0, the microscopic well depth increasing factor k_ε is proposed. It is assumed that the value of ε_0 between non-bonding molecules is ε_{st} under static loading, and the appearance of high strain rate under dynamic loading will cause the value of ε_0 to increase to ε_{dy}. In order to quantify the corresponding relationship between ε_{st} and ε_{dy}, the microscopic well depth increasing factor k_ε is proposed. The expression is written as

$$k_\varepsilon = \frac{\varepsilon_{dy}}{\varepsilon_{st}} \tag{1}$$

where ε_{st} represents the value of ε_0 under static loading (that is, when the strain rate effect is negligible), ε_{dy} represents the value of ε_0 under dynamic loading (that is, when the strain rate effect cannot be negligible).

2.3.2. Microscopic distance increasing factor k_r

High strain rate can affect not only the microscopic mechanical parameter ε_0, but also the microscopic mechanical parameter r_0. In order to quantify the effect of high strain rate on the microscopic mechanical parameters r_0, the microscopic distance increasing factor k_r is proposed. It is assumed that the value of r_0 between non-bonding molecules is r_{st} under static loading, and the appearance of high strain rate under dynamic loading will cause the value of r_0 to increase to r_{dy}. In order to quantify the corresponding relationship between r_{st} and r_{dy}, the microscopic distance increasing factor k_r is proposed. The expression is written as

$$k_r = \frac{r_{dy}}{r_{st}} \tag{2}$$

where r_{st} represents the value of r_0 under static loading (that is, when the strain rate effect is negligible), r_{dy} represents the value of r_0 under dynamic loading (that is, when the strain rate effect cannot be negligible).

Based on the microscopic mechanical parameters (ε_0 and r_0) of rocks under static loading and the newly defined two key parameters (k_ε and k_r), combined with the multi-scale model of rocks and the Lennard-Jones potential function, the force and potential energy functions are established during the dynamic tensile process and shear process.

2.4. Dynamic tensile process

In this section, for the dynamic tensile process of rocks, the force and potential energy functions of the strain-rate cohesive fracture model are established based on the Lennard-Jones potential and two key parameters (k_ε and k_r).

2.4.1. Research background

The failure of rocks in the semi-circular bend test is a typical tensile fracture process. When the loading rate of the external load F_L applied at the top of the semi-circular specimen is small, the failure of rocks can be considered as a static or quasi-static failure process without the influence of strain rate. With the gradual increase of loading rate, it can be considered that the failure of rocks gradually evolves from a static/quasi-static tensile failure to a dynamic tensile failure. Related studies have indicated that with the increase of

strain rate, the mechanical properties of rocks gradually increase.

In the process of dynamic tensile failure, the change in the position of molecules at the molecular scale in the multi-scale model is plotted in Fig. 3. When the external load F_L is applied at the top of the semi-circular specimen, the RVE at the tip of the pre-crack will undergo tensile deformation, causing the cementing substance between the mineral particles to undergo tensile deformation. Since the cementing substance at the particle scale is considered to be composed of a large number of neutral molecules at the molecular scale, the distance between molecules increases along with the tensile deformation of cementing substance. As the loading rate of the external load F_L increases, the strain rate effect gradually appears, which leads to the change of the microscopic mechanical parameters between non-bonding molecules, and further causes the macroscopic mechanical properties of rocks to change.

2.4.2. Potential energy function

For the Lennard-Jones potential energy of non-bonding molecules, related scholars proposed that when the intermolecular distance is greater than r_d, the intermolecular force and potential energy are negligible. To simplify the theoretical analysis, it is proposed that the cementing substance in the theoretical model of the rupture field is composed of 11 molecular layers. The potential energy of the entire rupture field is composed of the potential energy between any two molecular layers, and the two molecular layers may be adjacent or separated by 1–4 molecular layers. Next, the potential energy function between two molecular layers under different conditions during the dynamic tensile process is analyzed as follows.

Before establishing the potential energy function, some key parameters are first explained. The changing curves of Lennard-Jones potential w_{lj} and van der Waals force F_{vd} are plotted in Fig. 4, and the functions of w_{lj} and F_{vd} are written as Eq. (3) and Eq. (4). It is seen that there are four eigen values of r, r_0 denotes the distance at which w_{lj} is equal to 0, r_e denotes the distance at which F_{vd} is equal to 0 and w_{lj} attains the minimum value, r_s denotes the distance at which F_{vd} attains the maximum value, and r_d denotes the distance at which F_{vd} and w_{lj} are equal to 0. To distinguish the eigen values of r under static loading, the eigen values of r under dynamic loading are introduced, and r_{dye} denotes the distance at which F_{vd} is equal to 0 and w_{lj} attains the minimum value under dynamic loading.

For two adjacent molecular layers at the molecular scale, Lin proposed that the intermolecular distance is uniformly distributed from r_{min} to r_{max} at the initial moment of loading, and the values of r_{min} and r_{max} are obtained. As the distance between particles increases, the intermolecular distance at the molecular scale increases, and it is assumed that the increase in distance between any pair of molecules is Δr_v. Therefore, the intermolecular distance uniformly distributed within the range of $r_{min} + \Delta r_v$ to $r_{max} + \Delta r_v$. In addition, to obtain the potential energy and force between molecular layers, the number N_f^t of molecules in a molecular layer should be first determined, and it is written as Eq. (5). A more detailed introduction of these parameters can be found in the paper written by Lin. [61]

$$w_{lj} = 4\varepsilon_0[(\frac{r_0}{r})^{12} - (\frac{r_0}{r})^6] \tag{3}$$

$$F_{vd} = -\frac{dw_{lj}}{dr} = \frac{24\varepsilon_0}{r_0}[\frac{2r_0^{13}}{r^{13}} - \frac{r_0^7}{r^7}] \tag{4}$$

$$N_f^t = \frac{S_t\omega}{s_m} \tag{5}$$

where S_t denotes the boundary area of the rupture field in the theoretical model, ω denotes space occupancy ratio, s_m denotes the area occupied by a molecule.

For two molecular layers that are adjacent, the intermolecular distance is uniformly distributed from $r_{min} + \Delta r_v$ to $r_{max} + \Delta r_v$, and the potential energy W_{t0} between two molecular layers can be written as

$$W_{t0} = \sum_{i=1}^{N_f^t} w_{lj}(r_i) = \sum_{i=1}^{N_f^t} w_{lj}[(r_{min} + \Delta r_v) + \frac{i}{N_f^t}((r_{max} + \Delta r_v) - (r_{min} + \Delta r_v))] \tag{6}$$

Since N_f^t can be regarded as an infinite value, the cumulative form of W_{t0} is written as an integral form, which is written as

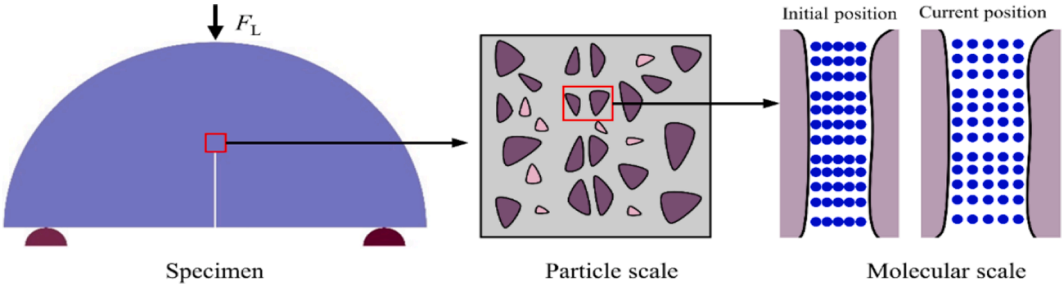

Fig. 3. Change in the position of molecules in the SCB test.

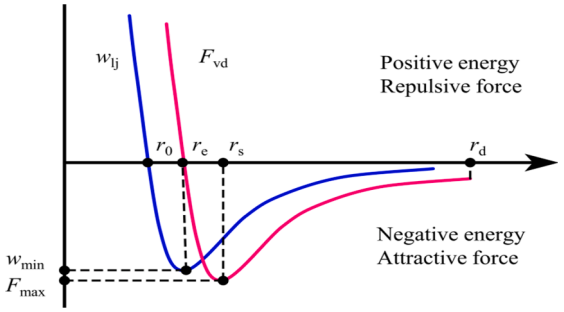

Fig. 4. Changing curves of Lennard-Jones potential w_{lj} and van der Waals force F_{vd}.

$$\begin{aligned} W_{t0} &= \int_{r_{min}+\Delta r_v}^{r_{max}+\Delta r_v} w_{lj}(r)\frac{N_f^t}{(r_{max}+\Delta r_v)-(r_{min}+\Delta r_v)}dr \\ &= \int_{r_{min}+\Delta r_v}^{r_{max}+\Delta r_v} 4k_\varepsilon\varepsilon_0\left(\frac{k_r^{12}r_0^{12}}{r^{12}}-\frac{k_r^6 r_0^6}{r^6}\right)\frac{N_f^t}{(r_{max}+\Delta r_v)-(r_{min}+\Delta r_v)}dr \\ &= \frac{4k_\varepsilon\varepsilon_0 N_f^t}{r_{max}-r_{min}}\left[\frac{1}{11}\left(\frac{k_r^{12}r_0^{12}}{(r_{min}+\Delta r_v)^{11}}-\frac{k_r^{12}r_0^{12}}{(r_{max}+\Delta r_v)^{11}}\right)+\frac{1}{5}\left(\frac{k_r^6 r_0^6}{(r_{max}+\Delta r_v)^5}-\frac{k_r^6 r_0^6}{(r_{min}+\Delta r_v)^5}\right)\right] \end{aligned} \tag{7}$$

For two molecular layers that are separated by i (i = 1, 2, 3 and 4) molecular layer, the intermolecular distance is uniformly distributed from $ir_{dye}+r_{min}+(i+1)\Delta r_v$ to $ir_{dye}+r_{max}+(i+1)\Delta r_v$, and the potential energy W_{ti} between two molecular layers is written as

$$\begin{aligned} W_{ti} &= \int_{ir_{dye}+r_{min}+(i+1)\Delta r_v}^{ir_{dye}+r_{max}+(i+1)\Delta r_v} 4k_\varepsilon\varepsilon_0\left(\frac{k_r^{12}r_0^{12}}{r^{12}}-\frac{k_r^6 r_0^6}{r^6}\right)\frac{N_f^t}{(ir_{dye}+r_{max}+(i+1)\Delta r_v)-(ir_{dye}+r_{min}+(i+1)\Delta r_v)}dr \\ &= \frac{4k_\varepsilon\varepsilon_0 N_f^t}{r_{max}-r_{min}}\left[\frac{1}{11}\left(\frac{k_r^{12}r_0^{12}}{(ir_{dye}+r_{min}+(i+1)\Delta r_v)^{11}}-\frac{k_r^{12}r_0^{12}}{(ir_{dye}+r_{max}+(i+1)\Delta r_v)^{11}}\right)\right. \\ &\quad \left.+\frac{1}{5}\left(\frac{k_r^6 r_0^6}{(ir_{dye}+r_{max}+(i+1)\Delta r_v)^5}-\frac{k_r^6 r_0^6}{(ir_{dye}+r_{min}+(i+1)\Delta r_v)^5}\right)\right] \end{aligned} \tag{8}$$

Based on Eq. (7) and Eq. (8), the potential energy W_t of the entire rupture field during the dynamic tensile process is obtained, and it is written as

$$\begin{aligned} W_t &= \frac{4k_\varepsilon\varepsilon_0 N_f^t\beta}{r_{max}-r_{min}}\sum_{i=0}^{4}\left\{(10-i)\left[\frac{1}{11}\left(\frac{k_r^{12}r_0^{12}}{(ir_{dye}+r_{min}+(i+1)\Delta r_v)^{11}}-\frac{k_r^{12}r_0^{12}}{(ir_{dye}+r_{max}+(i+1)\Delta r_v)^{11}}\right)\right.\right. \\ &\quad \left.\left.+\frac{1}{5}\left(\frac{k_r^6 r_0^6}{(ir_{dye}+r_{max}+(i+1)\Delta r_v)^5}-\frac{k_r^6 r_0^6}{(ir_{dye}+r_{min}+(i+1)\Delta r_v)^5}\right)\right]\right\} \end{aligned} \tag{9}$$

2.4.3. Force function

In the theoretical model of the rupture field, it is proposed that the cementing substance is composed of 11 molecular layers to simplify the theoretical analysis. Since it is determined that the intermolecular force is negligible when the intermolecular distance is greater than r_d, it can be concluded that the outermost molecular layer of the rupture field in the theoretical model bears the intermolecular force from other layers, and the two molecular layers may be adjacent or separated by 1–4 molecular layers. Next, the force function between two molecular layers under different conditions during the dynamic tensile process is analyzed as follows.

For two molecular layers that are adjacent, the intermolecular distance is uniformly distributed from $r_{min}+\Delta r_v$ to $r_{max}+\Delta r_v$, and the force F_{t0} between two molecular layers can be written as

$$F_{t0} = \sum_{i=1}^{N_f^t} F_{vd}(r_i) = \sum_{i=1}^{N_f^t} F_{vd}\left[(r_{min}+\Delta r_v)+\frac{i}{N_f^t}((r_{max}+\Delta r_v)-(r_{min}+\Delta r_v))\right] \tag{10}$$

Since N_f^t can be regarded as an infinite value, the cumulative form of F_{t0} is written as an integral form, which is written as

$$
\begin{aligned}
F_{t0} &= \int_{r_{min}+\Delta r_v}^{r_{max}+\Delta r_v} F_{vd}(r)\frac{N_f^t}{(r_{max}+\Delta r_v)-(r_{min}+\Delta r_v)}dr \\
&= \int_{r_{min}+\Delta r_v}^{r_{max}+\Delta r_v} \frac{24k_\varepsilon\varepsilon_0}{k_r r_0}\left(\frac{2k_r^{13}r_0^{13}}{r^{13}}-\frac{k_r^7 r_0^7}{r^7}\right)\frac{N_f^t}{(r_{max}+\Delta r_v)-(r_{min}+\Delta r_v)}dr \\
&= \frac{4k_\varepsilon\varepsilon_0 N_f^t}{r_{max}-r_{min}}\left[\left(\frac{-k_r^{12}r_0^{12}}{(r_{max}+\Delta r_v)^{12}}+\frac{k_r^{12}r_0^{12}}{(r_{min}+\Delta r_v)^{12}}\right)-\left(\frac{-k_r^6 r_0^6}{(r_{max}+\Delta r_v)^6}+\frac{k_r^6 r_0^6}{(r_{min}+\Delta r_v)^6}\right)\right]
\end{aligned}
\tag{11}
$$

For two molecular layers that are separated by i (i = 1, 2, 3 and 4) molecular layer, the intermolecular distance is uniformly distributed from $ir_{dye} + r_{min}$+$(i + 1)\Delta r_v$ to $ir_{dye} + r_{max}$+$(i + 1)\Delta r_v$, and the force F_{ti} between two molecular layers is written as

$$
\begin{aligned}
F_{ti} &= \int_{ir_{dye}+r_{max}+(i+1)\Delta r_v}^{ir_{dye}+r_{max}+(i+1)\Delta r_v} \frac{24k_\varepsilon\varepsilon_0}{k_r r_0}\left(\frac{2k_r^{13}r_0^{13}}{r^{13}}-\frac{k_r^7 r_0^7}{r^7}\right)\frac{N_f^t}{(ir_{dye}+r_{max}+(i+1)\Delta r_v)-(ir_{dye}+r_{min}+(i+1)\Delta r_v)}dr \\
&= \frac{4k_\varepsilon\varepsilon_0 N_f^t}{r_{max}-r_{min}}\left[\left(\frac{-k_r^{12}r_0^{12}}{(ir_{dye}+r_{max}+(i+1)\Delta r_v)^{12}}+\frac{k_r^{12}r_0^{12}}{(ir_{dye}+r_{min}+(i+1)\Delta r_v)^{12}}\right)\right. \\
&\quad \left.-\left(\frac{-k_r^6 r_0^6}{(ir_{dye}+r_{max}+(i+1)\Delta r_v)^6}+\frac{k_r^6 r_0^6}{(ir_{dye}+r_{min}+(i+1)\Delta r_v)^6}\right)\right]
\end{aligned}
\tag{12}
$$

Based on Eq. (11) and Eq. (12), the force F_t of the entire rupture field during the dynamic tensile process is obtained, and it is written as

$$
\begin{aligned}
F_t = \frac{4k_\varepsilon\varepsilon_0 N_f^t}{r_{max}-r_{min}}\sum_{i=0}^{4}\left\{\left[\frac{-k_r^{12}r_0^{12}}{(ir_{dye}+r_{max}+(i+1)\Delta r_v)^{12}}+\frac{k_r^{12}r_0^{12}}{(ir_{dye}+r_{min}+(i+1)\Delta r_v)^{12}}\right]\right. \\
\left.-\left[\frac{-k_r^6 r_0^6}{(ir_{dye}+r_{max}+(i+1)\Delta r_v)^6}+\frac{k_r^6 r_0^6}{(ir_{dye}+r_{min}+(i+1)\Delta r_v)^6}\right]\right\}
\end{aligned}
\tag{13}
$$

2.4.4. Effect of k_ε and k_r

The functions of potential energy W_t and force F_t are obtained based on theoretical analysis in Section 2.4.2 and Section 2.4.3. Because the corresponding relationship between displacement and force is often concerned in numerical simulations, this section focuses on the change characteristics of the tensile force–displacement curve when k_ε and k_r change.

When only the microscopic well depth increasing factor k_ε changes, the change characteristics of the tensile force–displacement curve are plotted in Fig. 5.

It can be observed that when k_r remains unchanged, with the increase of the k_ε, the maximum value F_{maxt} of dynamic tensile force F_t increases significantly, and F_{maxt} increases linearly with the increase of k_ε. However, the change trend of F_t with Δr_v has not changed significantly, and the corresponding Δr_v remains unchanged when F_t reaches the maximum value F_{maxt}.

When only the microscopic distance increasing factor k_r changes, the change characteristics of the tensile force–displacement curve are plotted in Fig. 6.

It can be observed that when k_ε remains unchanged, with the increase of k_r, the change trend of dynamic tensile force F_t changes significantly. Through the theoretical derivation of Eq. (13), it can be concluded that with the increase of k_r, the maximum value F_{maxt} of F_t decreases inversely, and the corresponding Δr_v increases linearly when F_t reaches the maximum value F_{maxt}.

When both the microscopic well depth increasing factor k_ε and microscopic distance increasing factor k_r changes, the change characteristics of the tensile force–displacement curve are plotted in Fig. 7.

Based on the corresponding relationship between k_ε and k_r, the change trend of dynamic tensile force F_t accompanying the changes of k_ε and k_r are explored for a total of three cases: $k_\varepsilon > k_r$ (Fig. 7(a)), $k_\varepsilon = k_r$ (Fig. 7(b)) and $k_\varepsilon < k_r$ (Fig. 7(c)). As can be seen from Fig. 7 (a), when $k_\varepsilon > k_r$, with the increase of k_ε and k_r, the change trend of the F_t-Δr_v curve changes. The maximum value F_{maxt} of F_t gradually decreases, while the Δr_v corresponding to F_{maxt} gradually increases. Based on Fig. 7(b), it can be found that when $k_\varepsilon = k_r$, with the increase of k_ε and k_r, the shape of the F_t-Δr_v curve changes to a certain extent. The maximum value F_{maxt} of F_t does not change, while

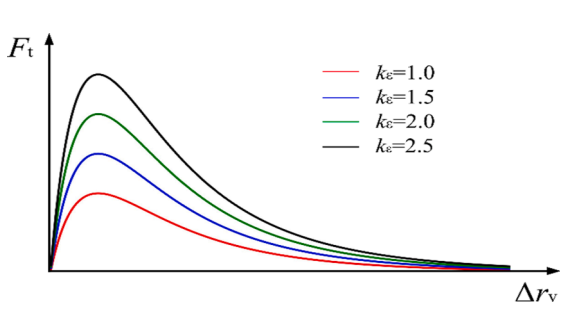

Fig. 5. Change characteristics of the tensile force–displacement curve when k_ε changes.

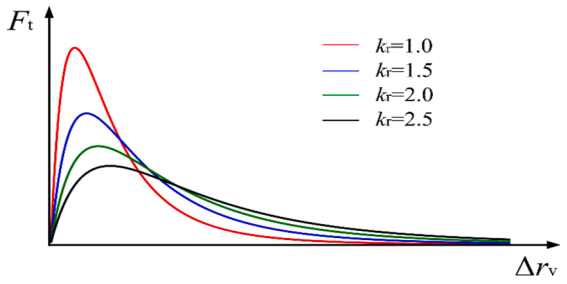

Fig. 6. Change characteristics of the tensile force–displacement curve when k_r changes.

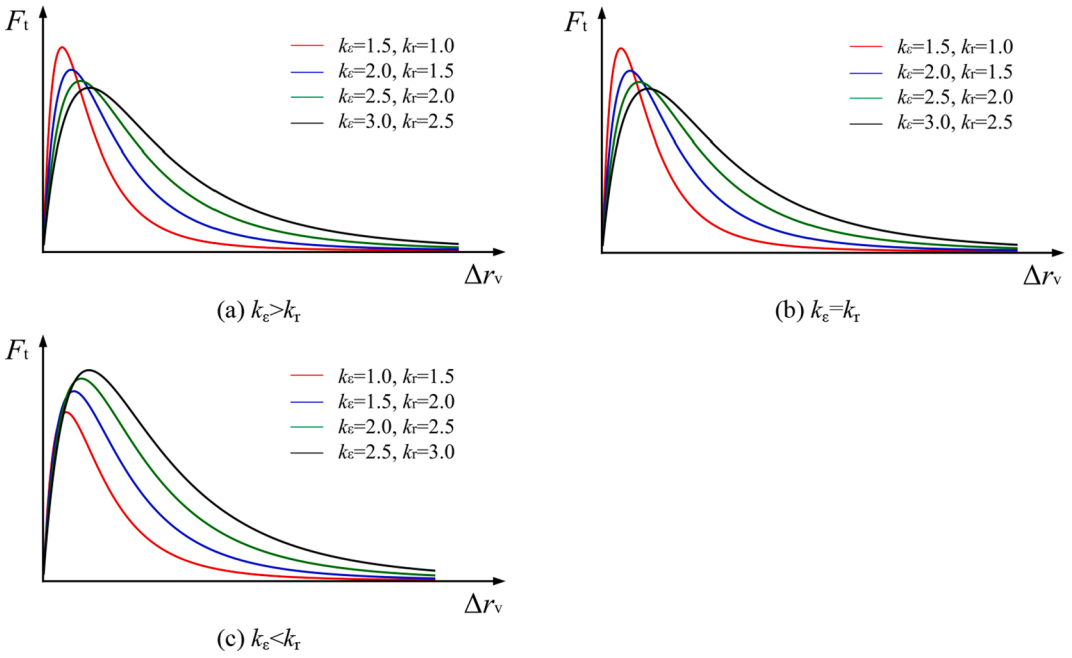

Fig. 7. Change characteristics of the tensile force–displacement curve when k_ε and k_r changes.

the Δr_v corresponding to F_{maxt} gradually increases. From Fig. 7(c), it can be concluded that when $k_\varepsilon < k_r$, with the increase of k_ε and k_r, the shape of the F_t-Δr_v curve does not change significantly. The maximum value F_{maxt} of F_t gradually increases, and the Δr_v corresponding to F_{maxt} gradually increases.

Through the theoretical derivation of Eq. (13), the corresponding relationship between the maximum value F_{maxt}^{dy} of the tensile force F_t in the dynamic tensile process and the maximum value F_{maxt}^{st} of the tensile force F_t in the static tensile process is written as

$$F_{maxt}^{dy} = \frac{k_\varepsilon}{k_r} F_{maxt}^{st} \tag{14}$$

Through the theoretical derivation of Eq. (9), the corresponding relationship between the tensile fracture energy G_t^{dy} in the dynamic tensile process and the tensile fracture energy G_t^{st} in the static tensile process is written as

$$G_t^{dy} = k_\varepsilon G_t^{st} \tag{15}$$

Based on Eq. (14) and Eq. (15), the values of k_ε and k_r at different strain rates can be obtained according to the macroscopic tensile fracture energy and tensile strength.

2.5. Dynamic shear process

In this section, for the dynamic shear process of rocks, the force and potential energy functions of the strain-rate cohesive fracture model are established based on the Lennard-Jones potential and two key parameters (k_ε and k_r).

2.5.1. Research background

The failure of rocks in the direct shear test is a typical shear fracture process. When the loading rate of the external load F_L applied at the upper part of the direct shear specimen is small, the failure of rocks can be considered as a static or quasi-static failure process without the influence of strain rate. With the gradual increase of loading rate, it can be considered that the failure of rocks gradually evolves from a static/quasi-static shear failure to a dynamic shear failure. Related studies have indicated that with the increase of strain rate, the mechanical properties of rocks gradually increase.

In the process of dynamic shear failure, the change in the position of molecules at the molecular scale in the multi-scale model is plotted in Fig. 8. When the external load F_L is applied at the upper part of specimen, the RVE at the shear plane undergoes shear deformation, causing the cementing substance between the mineral particles to undergo shear deformation. Since the cementing substance at the particle scale is considered to be composed of a large number of neutral molecules at the molecular scale, the shear distance between molecules at the molecular scale increases along with the shear deformation of cementing substance. As the loading rate of the external load F_L increases, the strain rate effect gradually appears, which leads to the change of the microscopic mechanical parameters between non-bonding molecules, and further causes the macroscopic mechanical properties of rocks to change.

In the theoretical analysis of the dynamic tensile process in Section 2.4, It is assumed that the intermolecular distance between the adjacent molecular layers is uniformly distributed from r_{min} to r_{max} at the initial moment of loading. However, to simplify the potential energy and force functions during the dynamic shear process, it is assumed that the intermolecular distance between the adjacent molecular layers is equal to r_{dye} at the initial moment of loading. Under this distribution condition, the total force between the adjacent molecular layers is still zero, which is consistent with the value when the intermolecular distance is uniformly distributed from r_{min} to r_{max}. But the value of potential energy is not consistent with the value of potential energy when the intermolecular distance is uniformly distributed from r_{min} to r_{max}. Therefore, a dimensionless coefficient η is proposed, and is written as [61]

$$\eta = \frac{w_{lj}(r_{dye})N_f^s}{\int_{r_{min}}^{r_{max}} w_{lj}(r)\frac{N_f^s}{r_{max}-r_{min}}dr} \approx 1.2566 \tag{16}$$

2.5.2. Potential energy function

To simplify the theoretical analysis of the dynamic shear process, it is proposed that the cementing substance in the theoretical model of the rupture field is composed of 11 molecular layers. The potential energy of the entire rupture field is composed of the potential energy between any two molecular layers, and the two molecular layers may be adjacent or separated by 1–4 molecular layers. Next, the potential energy function between two molecular layers under different conditions during the dynamic shear process is analyzed as follows.

For two molecular layers that are adjacent, the vertical intermolecular distance is r_{dye}, and the potential energy W_{s0} between two molecular layers is written as

$$W_{s0} = \frac{4k_\varepsilon\varepsilon_0 N_f^s}{\eta}\left[\left(\frac{k_r r_0}{\sqrt{r_{dye}^2 + (\Delta r_u)^2}}\right)^{12} - \left(\frac{k_r r_0}{\sqrt{r_{dye}^2 + (\Delta r_u)^2}}\right)^{6}\right] \tag{17}$$

For two molecular layers that are separated by i ($i = 1, 2, 3$ and 4) molecular layer, the vertical intermolecular distance is $(i+1)r_{dye}$, and the potential energy W_{si} between two molecular layers is written as

$$W_{si} = \frac{4k_\varepsilon\varepsilon_0 N_f^s}{\eta}\left[\left(\frac{k_r r_0}{\sqrt{((i+1)r_{dye})^2 + ((i+1)\Delta r_u)^2}}\right)^{12} - \left(\frac{k_r r_0}{\sqrt{((i+1)r_{dye})^2 + ((i+1)\Delta r_u)^2}}\right)^{6}\right] \tag{18}$$

Based on Eq. (17) and Eq. (18), the potential energy W_s of the entire rupture field during the dynamic shear process is obtained, and it is written as

$$W_s = \frac{4k_\varepsilon\varepsilon_0 N_f^s\beta}{\eta}\sum_{i=0}^{4}\left\{(10-i)\left[\left(\frac{k_r r_0}{\sqrt{((i+1)r_{dye})^2 + ((i+1)\Delta r_u)^2}}\right)^{12} - \left(\frac{k_r r_0}{\sqrt{((i+1)r_{dye})^2 + ((i+1)\Delta r_u)^2}}\right)^{6}\right]\right\} \tag{19}$$

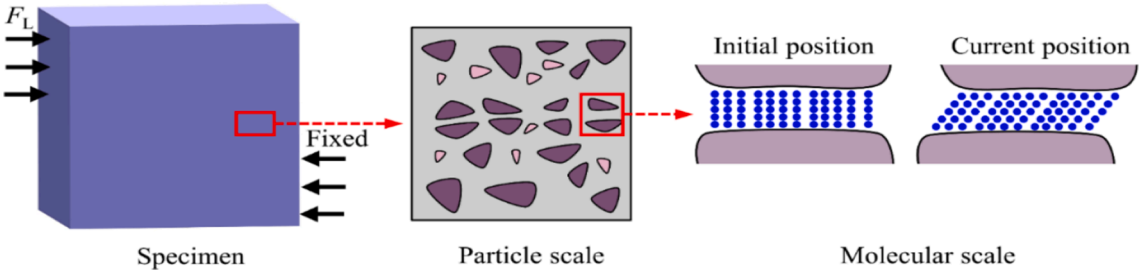

Fig. 8. Change in the position of molecules in the direct shear test.

2.5.3. Force function

In the theoretical model of the rupture field, it is proposed that the cementing substance is composed of 11 molecular layers to simplify the theoretical analysis. Since it is determined that the intermolecular force is negligible when the intermolecular distance is greater than r_d, it can be concluded that the outermost molecular layer of the rupture field in the theoretical model bears the intermolecular force from other layers, and the two molecular layers may be adjacent or separated by 1–4 molecular layers. Next, the force function between two molecular layers under different conditions during the dynamic shear process is analyzed as follows.

For two molecular layers that are adjacent, the vertical intermolecular distance is r_{dye}, and the force F_{s0} between two molecular layers is written as

$$F_{s0} = \frac{24k_\varepsilon\varepsilon_0\Delta r_u N_f^s}{\eta k_r r_0 r_{dy}}\left[\frac{2k_r^{13}r_0^{13}}{\left(r_{dye}^2+(\Delta r_u)^2\right)^{\frac{13}{2}}}-\frac{k_r^7 r_0^7}{\left(r_{dye}^2+(\Delta r_u)^2\right)^{\frac{7}{2}}}\right] \tag{20}$$

For two molecular layers that are separated by i ($i = 1, 2, 3$ and 4) molecular layer, the vertical intermolecular distance is $(i+1)r_{dye}$, and the force F_{si} between two molecular layers is written as

$$F_{si} = \frac{24k_\varepsilon\varepsilon_0\Delta r_u N_f^s}{\eta k_r r_0 r_{dy}}\left[\frac{2k_r^{13}r_0^{13}}{\left(((i+1)r_{dye})^2+((i+1)\Delta r_u)^2\right)^{\frac{13}{2}}}-\frac{k_r^7 r_0^7}{\left(((i+1)r_{dye})^2+((i+1)\Delta r_u)^2\right)^{\frac{7}{2}}}\right] \tag{21}$$

Based on Eq. (20) and Eq. (21), the force F_s of the entire rupture field during the dynamic shear process is obtained, and it is written as

$$F_s = \frac{24k_\varepsilon\varepsilon_0\Delta r_u N_f^s}{\eta k_r r_0 r_{dy}}\sum_{i=0}^{4}\left\{\frac{2k_r^{13}r_0^{13}}{\left[((i+1)r_{dye})^2+((i+1)\Delta r_u)^2\right]^{\frac{13}{2}}}-\frac{k_r^7 r_0^7}{\left[((i+1)r_{dye})^2+((i+1)\Delta r_u)^2\right]^{\frac{7}{2}}}\right\} \tag{22}$$

2.5.4. Effect of k_ε and k_r

The functions of potential energy W_s and force F_s are obtained based on theoretical analysis in Section 2.5.2 and Section 2.5.3. Because the corresponding relationship between displacement and force is often concerned in numerical simulations, this section focuses on the change characteristics of the shear force–displacement curve when k_ε and k_r change.

When only the microscopic well depth increasing factor k_ε changes, the change characteristics of the shear force–displacement curve are plotted in Fig. 9.

It can be observed that when k_r remains unchanged, with the increase of the k_ε, the maximum value F_{maxs} of dynamic shear force F_s increases significantly, and F_{maxs} increases linearly with the increase of k_ε. However, the change trend of F_s with Δr_u has not changed significantly, and the corresponding Δr_u remains unchanged when F_s reaches the maximum value F_{maxs}.

When only the microscopic distance increasing factor k_r changes, the change characteristics of the shear force–displacement curve are plotted in Fig. 10.

It can be observed that when k_ε remains unchanged, with the increase of k_r, the change trend of dynamic shear force F_s changes significantly. Through the theoretical derivation of Eq. (22), it can be concluded that with the increase of k_r, the maximum value F_{maxs} of F_s decreases inversely, and the corresponding Δr_u increases linearly when F_s reaches the maximum value F_{maxs}.

When both the microscopic well depth increasing factor k_ε and microscopic distance increasing factor k_r changes, the change characteristics of the shear force–displacement curve are plotted in Fig. 11.

Based on the corresponding relationship between k_ε and k_r, the change trend of dynamic shear force F_s accompanying the changes of k_ε and k_r are explored for a total of three cases: $k_\varepsilon > k_r$ (Fig. 11(a)), $k_\varepsilon = k_r$ (Fig. 11(b)) and $k_\varepsilon < k_r$ (Fig. 11(c)). As can be seen from Fig. 11(a), when $k_\varepsilon > k_r$, with the increase of k_ε and k_r, the change trend of the F_s-Δr_u curve changes. The maximum value F_{maxs} of F_s gradually decreases, while the Δr_u corresponding to F_{maxs} gradually increases. Based on Fig. 11(b), it can be found that when $k_\varepsilon = k_r$, with the increase of k_ε and k_r, the shape of the F_s-Δr_u curve changes to a certain extent. The maximum value F_{maxs} of F_s does not change, while the Δr_u corresponding to F_{maxs} gradually increases. From Fig. 11(c), it can be concluded that when $k_\varepsilon < k_r$, with the increase of k_ε and k_r, the shape of the F_s-Δr_u curve does not change significantly. The maximum value F_{maxs} of F_s gradually increases, and the Δr_u corresponding to F_{maxs} gradually increases.

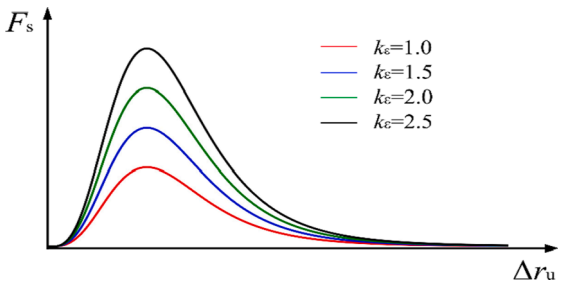

Fig. 9. Change characteristics of the shear force–displacement curve when k_ε changes.

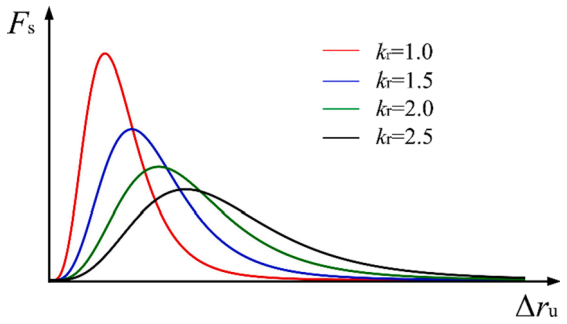

Fig. 10. Change characteristics of the shear force–displacement curve when k_r changes.

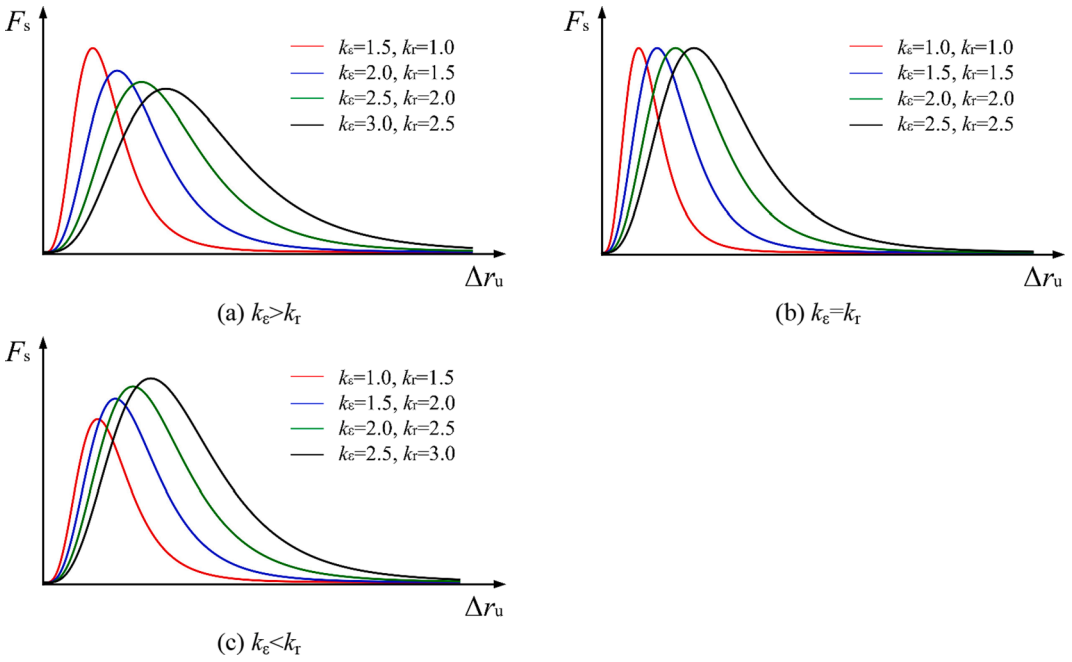

Fig. 11. Change characteristics of the shear force–displacement curve when k_ε and k_r changes.

Through the theoretical derivation of Eq. (22), the corresponding relationship between the maximum value F_{maxs}^{dy} of the shear force F_s in the dynamic shear process and the maximum value F_{maxs}^{st} of the shear force F_s in the static shear process is written as

$$F_{maxs}^{dy} = \frac{k_\varepsilon}{k_r} F_{maxs}^{st} \tag{23}$$

Through the theoretical derivation of Eq. (19), the corresponding relationship between the shear fracture energy G_s^{dy} in the dynamic shear process and the shear fracture energy G_s^{st} in the static shear process is written as

$$G_s^{dy} = k_\varepsilon G_s^{st} \tag{24}$$

Based on Eq. (23) and Eq. (24), the values of k_ε and k_r at different strain rates can be obtained according to the macroscopic shear fracture energy and shear strength.

3. Numerical implementation

To verify the accuracy of the strain-rate cohesive fracture model in simulating the dynamic failure process of rocks, numerical simulations are conducted by introducing the newly proposed model into the Continuum Discontinuum Element Method (CDEM).

3.1. Introduction of CDEM

The continuum discontinuum element method (CDEM) is a dynamic explicit numerical algorithm under the Lagrangian system. In this algorithm, a strict control equation is first established based on the Lagrangian energy system, and the dynamic relaxation method is used for explicit iterative solution, thereby a unified continuous-discontinuous description is achieved. The fracture separation at the block boundaries and inside the block is used to simulate the progressive damage process of materials, thus realizing the numerical simulation of the whole process of materials from continuous deformation to fracture until movement. The continuum discontinuum element method combines the advantages of continuous simulation and discrete simulation. The continuous simulation can be conducted by using finite element method, finite volume method and spring element method, and discrete simulation can be conducted by using the discrete element method. [65–68]

The basic numerical model in CDEM includes block and interface, as shown in Fig. 12, which represent different characteristics of materials. For the block, it is used to characterize the continuous features of materials, and each block is composed of one or more finite element elements. For the interface, it is the common boundary of two blocks, which is used to characterize the discontinuous features of materials, such as fracture and collision. The interface in CDEM is composed of the real interface (denoted by the black solid lines in Fig. 12) and the virtual interface (denoted by the red dotted lines in Fig. 12). The real interface represents the real discontinuous features of materials, such as joints and faults in geological bodies. The virtual interface has two main functionalities: to connect blocks and transfer mechanical information, and to provide the potential space for crack initiation and propagation. [69]

The time-based dynamic relaxation method is adopted by CDEM to conduct explicit iterative calculation, which has obvious advantages in solving dynamic problems, nonlinear problems, and large displacement problems. The calculation flow is plotted in Fig. 13. First, the acceleration, velocity and displacement of nodes are calculated. Subsequently, the deformation force of elements is calculated, followed by obtaining the resultant force of nodes. Finally, the unbalance ratio of the entire system is calculated, and it is determined whether to terminate the iterative calculation. Since the numerical model of CDEM includes block and interface, the constitutive model includes the constitutive model of block and the constitutive model of interface when calculating the deformation force based on the constitutive model. The strain-rate cohesive fracture model proposed in this paper is a new constitutive model of interface (the red part in Fig. 13). In order to verify the accuracy of the newly proposed model in simulating the dynamic fracture process of rocks, the constitutive model is written as a C++ code and embedded into the CDEM calculation flow by using the secondary development function of CDEM.

3.2. Numerical model verification

To verify the accuracy of the strain-rate cohesive fracture model in simulating the rock fracture process under dynamic loading, numerical simulation corresponding to dynamic axial tensile test, dynamic Brazilian disc test and dynamic uniaxial compression test is conducted.

3.2.1. Dynamic tensile test

In the dynamic axial tensile test, the rock specimen will undergo tensile failure. In order to verify the accuracy of the strain-rate cohesive fracture model in simulating dynamic tensile fracture, a comparative analysis between numerical results and experimental results of dynamic axial tensile test is carried out.

Based on the MTS-810NEW servo-hydraulic machine, Zhong [70] studied the fracture performance of rock specimen subjected to tensile loading at four strain rates of 10^{-6} s^{-1}, 10^{-5} s^{-1}, 10^{-4} s^{-1} and 10^{-3} s^{-1}, and obtained the peak force and fracture energy of specimen at different strain rates. The size of rock specimen is 200 mm × 100 mm × 100 mm, and the middle of specimen is bilaterally with prefabricated cracks (seam depth 15 mm). The numerical model is plotted in Fig. 14, and a tensile velocity is applied at the top and bottom boundaries of the numerical model. The common boundaries between elements are set as virtual interfaces, and the strain-rate cohesive fracture model is adopted as the constitutive model of interfaces. The mechanical parameters of rock specimen are quoted from Zhong, and they are shown in Table 1.

At four different strain rates of 10^{-6} s^{-1}, 10^{-5} s^{-1}, 10^{-4} s^{-1} and 10^{-3} s^{-1}, the peak force of rock specimen obtained by the laboratory test and numerical simulation is plotted in Fig. 15. The horizontal axis denotes the logarithm of the ratio of strain rate to 10^{-6}, and the vertical axis denotes the peak force. It can be seen that the peak force presents obviously rate-dependent, which increases

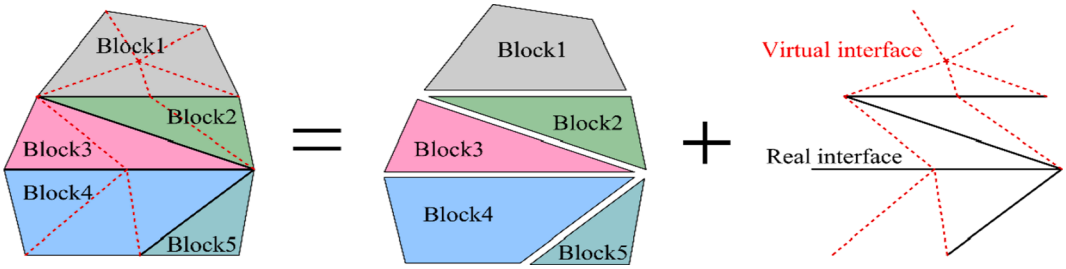

Fig. 12. Block and interface in CDEM.

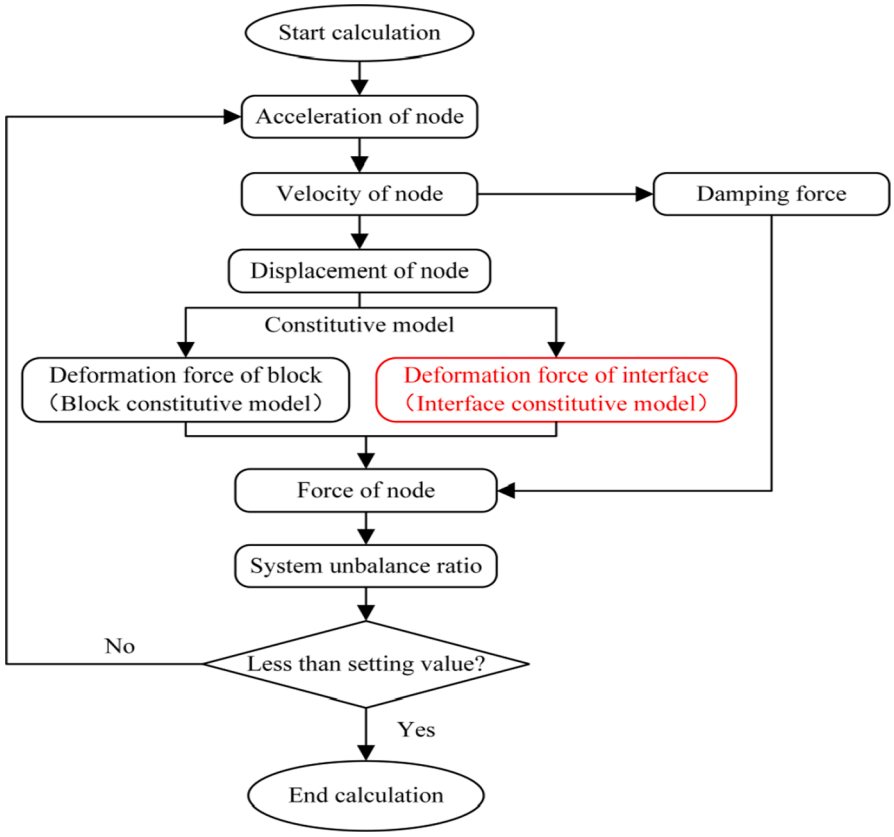

Fig. 13. Schematic diagram of the calculation flow in CDEM.

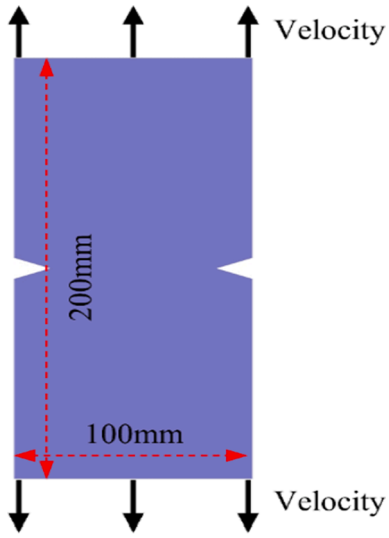

Fig. 14. Numerical model of dynamic axial tensile test.

significantly with the increase of strain rate. The change trend of peak force obtained by the numerical simulation is consistent with the change trend of peak force obtained by the laboratory test. With the increase of $log(\dot{\varepsilon}/10^{-6})$, the peak force increases approximately linearly, and the maximum error of peak force obtained by numerical simulation and laboratory test is 3.83%.

The fitting function of the peak force F_p obtained by laboratory test is written as

Table 1
Static mechanical parameters of rock.

Density kg/m^3	Elastic modulus GPa	Poisson's ratio	Tensile strength MPa	Tensile fracture energy J
2710	50.3	0.23	3.54	57.29

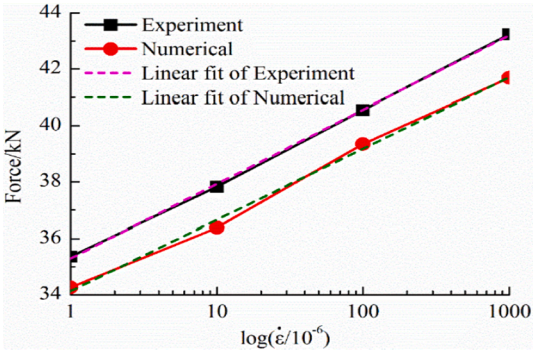

Fig. 15. Relationship between peak force and strain rate.

$$F_p = 35.292 + 2.637log(\dot{\varepsilon}/10^{-6}) \tag{25}$$

The fitting function of the peak force F_p obtained by numerical simulation is written as

$$F_p = 34.131 + 2.526log(\dot{\varepsilon}/10^{-6}) \tag{26}$$

To further investigate the change trend of fracture energy of rock specimen at different strain rates, the displacement-force curve of the numerical spring at the virtual interface is plotted in Fig. 16. The horizontal axis represents the tensile displacement of the numerical spring, and the vertical axis represents the tensile force of the numerical spring. From Fig. 16, it can be concluded that the shape of the displacement-force curve at different strain rates is similar, but the peak force of the numerical spring shows obviously rate-dependent. As the strain rate increases, the peak force gradually increases. The area under the displacement-force curve denotes the tensile fracture energy of numerical spring, and the change trend of tensile fracture energy at different strain rates is shown in Fig. 17. It can be concluded that the tensile fracture energy presents obviously rate-dependent, and the fracture energy increases significantly with the increase of strain rate. The change trend of the tensile fracture energy obtained by numerical simulation and the change trend of the tensile fracture energy obtained by laboratory test remain consistent, and the error between numerical results and experiment results is the largest at 0.1% for a strain rate of 10^{-5}.

To further investigate the accuracy of the strain-rate cohesive fracture model in simulating dynamic tensile fracture, the dynamic Brazilian disc test is simulated. Yang [71] conducted the dynamic splitting tensile test of Brazilian disc specimens at different impact velocities, and obtained the relevant dynamic tensile mechanical parameters. The dynamic Brazilian disc test for granite is simulated, and the differences between numerical results and experimental results are compared.

Based on the Split Hopkinson pressure bar system (SHPB), Yang estimated the fracture performance of granite at three loading rate of 144 GPa·s^{-1}, 350 GPa·s^{-1} and 660 GPa·s^{-1}, and obtained the dynamic tensile strength. The granite specimen is a cylinder, with a dimension of 25 mm × Φ 50 mm. The common boundaries between elements are set as virtual interfaces, and the strain-rate cohesive

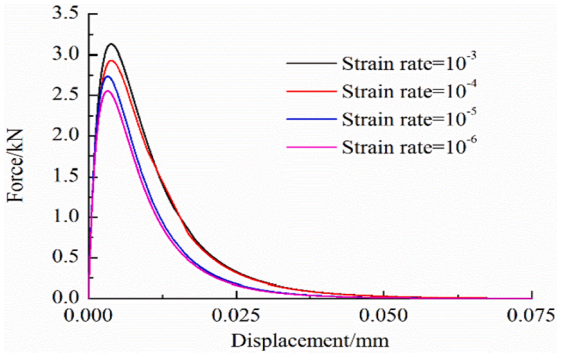

Fig. 16. Displacement-force curve of the numerical spring at different strain rates.

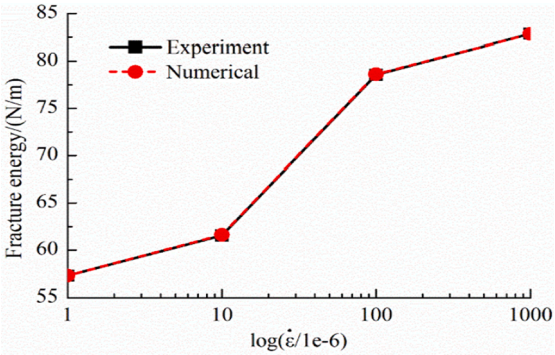

Fig. 17. Relationship between fracture energy and strain rate.

fracture model is adopted as the constitutive model of interfaces. The static mechanical parameters of granite are shown in Table 2.

At loading rate of 144 GPa·s^{-1}, 350 GPa·s^{-1} and 660 GPa·s^{-1}, the dynamic tensile strength of granite obtained by the laboratory test and numerical simulation is plotted in Fig. 18. The horizontal axis denotes the loading rate, and the vertical axis denotes the dynamic tensile strength. It is seen that the change trend of dynamic tensile strength obtained by experiment and numerical simulation is similar, the dynamic tensile strength gradually increases with the increase of loading rate. At the loading rate of 660 GPa·s^{-1}, the dynamic tensile strength obtained by experiment is $\sigma_{te} = 20.50$ MPa, the dynamic tensile strength obtained by numerical simulation is $\sigma_{tn} = 18.60$ MPa, and the error between experiment result and numerical result is 9.27%.

Based on the comparison of numerical results and experimental results in dynamic axial tensile test and dynamic Brazilian disc test, the accuracy of the strain-rate cohesive fracture model in simulating the dynamic tensile failure is verified.

3.2.2. *Dynamic compression test*

In the dynamic uniaxial compression test, the rock mainly undergoes shear fracture. In order to verify the accuracy of the strain-rate cohesive fracture model in simulating the dynamic shear fracture process, a comparative analysis of the numerical results and experimental results of the dynamic compression test is carried out.

Wang [72] carried out uniaxial compression tests under static and dynamic loading for Baoxing marble, and obtained the stress–strain curves of rocks at different strain rates. For the uniaxial compression test of marble under static loading, an electronic universal testing machine UTM5305 is adopted to carry out laboratory test. For the uniaxial compression test of marble under dynamic loading, it is carried out with a 20 mm diameter Split Hopkinson pressure bar system (SHPB). By adjusting the air pressure, the dynamic failure of rock specimen at different strain rates can be realized. The numerical model is plotted in Fig. 19, with a dimension of 18.6 mm × Φ 9.3 mm. The numerical model is discretized into a series of tetrahedral elements, and the common boundaries of the elements are set as virtual interfaces. The static mechanical parameters of Baoxing marble are shown in Table 3.

The numerical simulation of uniaxial compression test under static loading is conducted first, and the stress–strain curve is plotted in Fig. 20. Since the strain rate effect in uniaxial compression test can be neglected, the static cohesive fracture model is adopted as the interface constitutive model. It can be seen that the stress–strain curve obtained by numerical simulation is consistent with that obtained by laboratory test. In the initial stage of loading, with the increase of compressive strain, the stress increases approximately linearly. When the stress reaches the peak value, with the increase of strain, the stress decreases rapidly. In the laboratory test, when the compressive strain reaches 0.54%, the compressive stress reaches the peak value of 102.73 MPa. In the numerical simulation, when the compressive strain reaches 0.53%, the compressive stress reaches the peak value of 107.02 MPa. For the peak value of compressive stress, the error between experiment result and numerical result is 4.01%. Therefore, it can be determined that the strain-rate cohesive fracture model can accurately simulate the shear failure process of rocks in the static compression test.

Subsequently, the numerical simulation of uniaxial compression test under dynamic loading is conducted. Based on the Split Hopkinson pressure bar system, Wang obtained the dynamic stress–strain curve of Baoxing marble at different strain rates by adjusting the air pressure, and obtained the relevant mechanical parameter values. Based on the available mechanical parameters, numerical simulation of uniaxial compression failure process of rocks at high strain rates is carried out.

The main components in the SHPB system are shown in Fig. 21. The length of the incident bar and transmission bar is 1.5 m, the diameter is 0.02 m. The dimension of rock specimen is 18.6 mm × Φ 9.3 mm. When the sticker bar hits the incident bar, a dynamic compressive wave (incident wave ε_i) will be activated. When the incident wave ε_i propagate within the incident bar, once the wave reaches the right end, one part of incident wave is reflected (reflected wave ε_r) because of the mismatch of surge impedance of rock specimen and incident bar, and another part passes through the rock specimen generating a transmission wave ε_t. Wang does not provide the velocity of the sticker bar for different strain rates, but gave the value of incident strain wave ε_i monitored in the middle of the incident bar. Therefore, the sticker bar is not established in the numerical model of SHPB, and a dynamic stress wave is directly applied at the incident bar to simulate the impact effect of the sticker bar on the incident bar.

To verify the accuracy of the dynamic stress wave applied at the incident bar, a comparison of the strain wave value in the middle of the incident bar at a strain rate of 200 s^{-1} is first carried out, as shown in Fig. 22, the negative value indicates compressive strain. The nephogram of incident stress wave within the incident bar is plotted in Fig. 23, and the negative value indicates compressive stress. It

Table 2
Static mechanical parameters of granite.

Material	Density kg/m^3	Elastic modulus GPa	Tensile strength MPa	Uniaxial compressive strength MPa
granite	2630	16.25	6.82	126

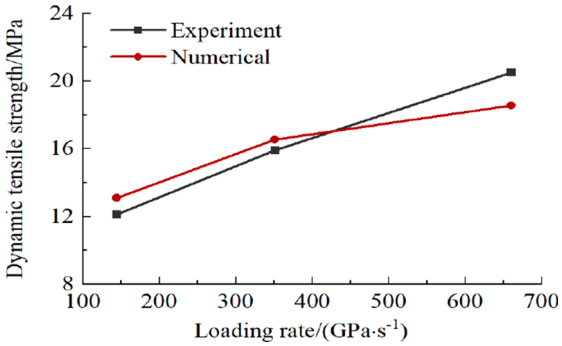

Fig. 18. Dynamic tensile strength of granite at different loading rate.

Fig. 19. Numerical model of dynamic compression test.

Table 3
Static mechanical parameters of Baoxing marble.

Density kg/m^3	Elasticity GPa	Tensile strength MPa	Cohesive strength MPa	Friction angle
2600	20	8	14	45

can be concluded that the strain wave monitored by the test and the strain wave obtained by the numerical simulation agree when the strain rate is 200 s^{-1}. Not only the value of the strain wave is similar, but also the duration of the strain wave is similar. Therefore, the accuracy of the applied incident stress wave can be determined. Based on the value of the incident stress wave at 200 s^{-1}, the incident waveform at other strain rates is converted proportionally.

The stress–strain curves for dynamic uniaxial compression tests of rocks at different strain rates are plotted in Fig. 24. It can be concluded that for any strain rate, the change trends of stress–strain curves obtained by numerical simulation and laboratory test are

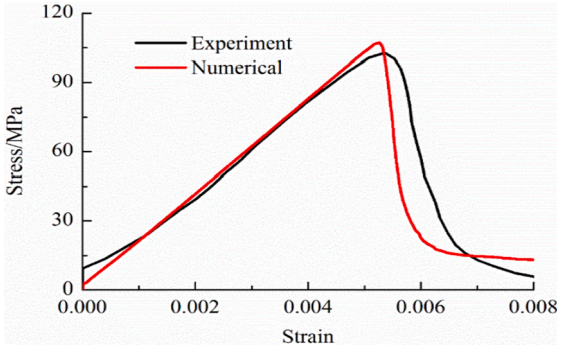

Fig. 20. Stress–strain curve in static uniaxial compression test.

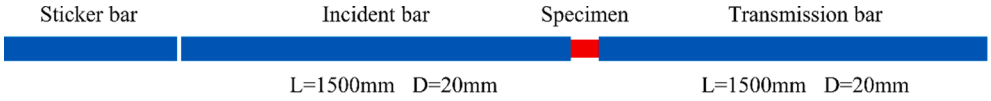

Fig. 21. Main components in the SHPB system.

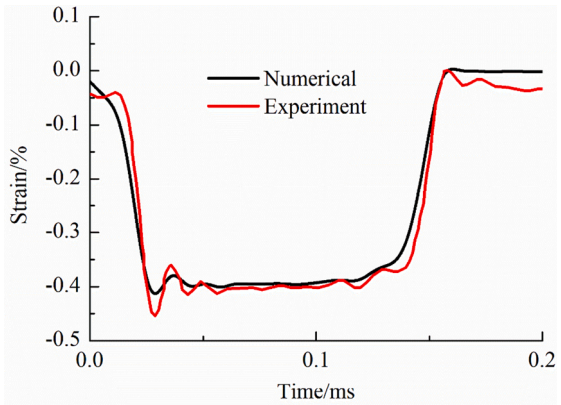

Fig. 22. Incident strain wave at the strain rate of 200 s^{-1}.

basically the same. In the initial stage of loading, with the increase of compressive strain, the compressive stress gradually increases, but the stress increases at different speeds at different strain rates. As the strain rate increases, the compressive stress increases faster. When the stress reaches the peak value, the stress gradually decreases as the strain increases. When the strain rate is 400 s^{-1}, the error between the peak stress obtained by numerical simulation and the peak stress obtained by test is the largest, which is 7.60%.

The accuracy of the strain-rate cohesive fracture model in simulating dynamic shear fracture is verified based on the simulation of static and dynamic uniaxial compression tests of Baoxing marble.

4. Conclusions

The strain-rate cohesive fracture model is established to characterize the dynamic mechanical response of rocks at high strain rates. First, the newly proposed model explains the microscopic mechanism of the strain rate effect from the molecular scale and defines microscopic dynamic increasing factor k_ε and k_r. Then, the potential energy and force functions corresponding to the dynamic tensile and shear processes are established. Finally, the accuracy of the newly proposed model is verified based on the numerical results of dynamic tensile test and dynamic compression test. The following conclusions can be drawn:

1) The essence of the strain rate effect is that the high strain rate leads to changes in the microscopic mechanical parameters between non-bonding molecules, which in turn leads to changes in the macroscopic mechanical properties of materials at different strain rates.

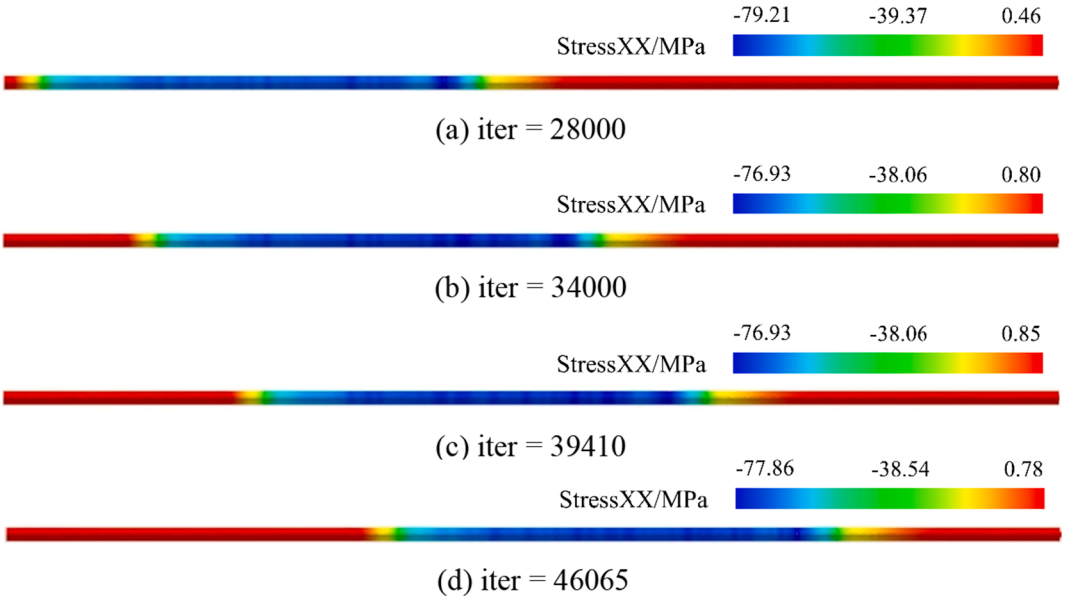

Fig. 23. Nephogram of incident stress wave within the incident bar.

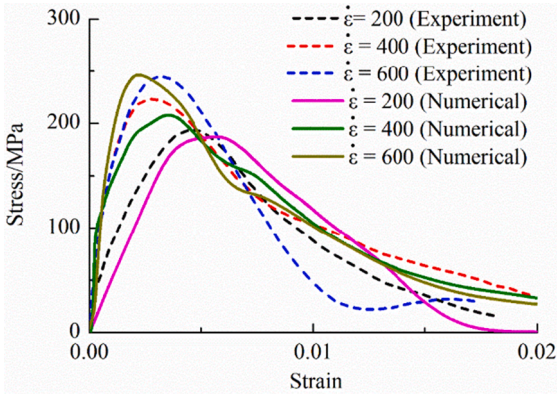

Fig. 24. Stress–strain curves at different strain rates.

2) Both microscopic dynamic increasing factors k_e and k_r affect the displacement-force curve. When only k_e increases, the peak value of force changes, but the failure displacement corresponding to the peak value remains unchanged. When only k_r changes, both the peak value of force and the failure displacement corresponding to the peak value change.
3) Based on the comparative analysis of dynamic axial tensile test, dynamic Brazilian disc test and dynamic compression test, it is concluded that the strain-rate cohesive fracture model can accurately simulate not only the dynamic tensile fracture process of rocks under dynamic tensile loading, but also the dynamic shear fracture process of rocks under dynamic compressive loading.

Data availability statement

Data in this manuscript is good to offer, is there is any request, please contact Corresponding Author.

Declaration of Competing Interest

The authors declare that they have no known competing financial interests or personal relationships that could have appeared to influence the work reported in this paper.

Acknowledgements

The authors would like to acknowledge the financial support of the National Key Research and Development Project of China, the

Ministry of Science and Technology of China (Project No. 2018YFC1505504).

References

[1] Blondeau S, Gunnell Y, Jarman D. Rock slope failure in the Western Alps: A first comprehensive inventory and spatial analysis. Geomorphology 2021;380:107622. https://doi.org/10.1016/j.geomorph.2021.107622.

[2] Geng J, Chen W-y. Analysis on deformation mechanism of high rock slope of hydropower station under complex hydrogeology. Microprocess Microsyst 2021;81:103733. https://doi.org/10.1016/j.micpro.2020.103733.

[3] Ju Y, Wang Y, Su C, Zhang D, Ren Z. Numerical analysis of the dynamic evolution of mining-induced stresses and fractures in multilayered rock strata using continuum-based discrete element methods. Int J Rock Mech Min Sci 2019;113:191–210.

[4] Wang L, Lu Z, Chen D-P, Liu Q-Q, Chu P, Shu L-Y, et al. Safe strategy for coal and gas outburst prevention in deep-and-thick coal seams using a soft rock protective layer mining. Saf Sci 2020;129:104800. https://doi.org/10.1016/j.ssci.2020.104800.

[5] Zhao Y, Yang T, Liu H, Wang S, Zhang P, Jia P, et al. A path for evaluating the mechanical response of rock masses based on deep mining-induced microseismic data: A case study. Tunn Undergr Space Technol 2021;115:104025. https://doi.org/10.1016/j.tust.2021.104025.

[6] Bai C, Xue Y, Qiu D, Su M, Ma X, Liu H. Analysis of factors affecting the deformation of soft rock tunnels by data envelopment analysis and a risk assessment model. Tunn Undergr Space Technol 2021;116:104111. https://doi.org/10.1016/j.tust.2021.104111.

[7] Li X, Zhu Z, Wang M, Xiao D, Shu Y, Deng S. Fracture mechanism of rock around a tunnel-shaped cavity with interconnected cracks under blasting stress waves. Int J Impact Engng 2021;157:103999. https://doi.org/10.1016/j.ijimpeng.2021.103999.

[8] Zhao H, Chen B, Li S, Li Z, Zhu C. Updating the models and uncertainty of mechanical parameters for rock tunnels using Bayesian inference. Geosci Front 2021;12(5):101198. https://doi.org/10.1016/j.gsf.2021.101198.

[9] Vervoort A, Min K-B, Konietzky H, Cho J-W, Debecker B, Dinh Q-D, et al. Failure of transversely isotropic rock under Brazilian test conditions. Int J Rock Mech Min Sci 2014;70:343–52.

[10] Kataoka M, Mahdavi E, Funatsu T, Takehara T, Obara Y, Fukui K, et al. Estimation of Mode I fracture toughness of rock by semi-circular bend test under confining pressure condition. Procedia Engng 2017;191:886–93.

[11] Fan X, Jiang X, Liu Y, Lin H, Li K, He Z. Local stress distribution and evolution surrounding flaw and opening within rock block under uniaxial compression. Theor Appl Fract Mech 2021;112:102914. https://doi.org/10.1016/j.tafmec.2021.102914.

[12] Li N, Zou Y, Zhang S, Ma X, Zhu X, Li S, et al. Rock brittleness evaluation based on energy dissipation under triaxial compression. J Petrol Sci Engng 2019;183:106349. https://doi.org/10.1016/j.petrol.2019.106349.

[13] Weilv W, Xu W, Jianpin Z. Effect of inclined interface angle on shear strength and deformation response of cemented paste backfill-rock under triaxial compression. Constr Build Mater 2021;279:122478. https://doi.org/10.1016/j.conbuildmat.2021.122478.

[14] Sanei M, Faramarzi L, Fahimifar A, Goli S, Mehinrad A, Rahmati A. Shear strength of discontinuities in sedimentary rock masses based on direct shear tests. Int J Rock Mech Min Sci 2015;75:119–31.

[15] Wang Y, Deng H, Deng Y, Chen K, He J. Study on crack dynamic evolution and damage-fracture mechanism of rock with pre-existing cracks based on acoustic emission location. J Petrol Sci Engng 2021;201:108420. https://doi.org/10.1016/j.petrol.2021.108420.

[16] Rahman T, Lebedev M, Zhang Y, Barifcani A, Iglauer S. Influence of rock microstructure on its electrical properties: an analysis using X-ray microcomputed tomography. Energy Procedia 2017;114:5023–31.

[17] Wang Y, Feng WK, Wang HJ, Li CH, Hou ZQ. Rock bridge fracturing characteristics in granite induced by freeze-thaw and uniaxial deformation revealed by AE monitoring and post-test CT scanning. Cold Reg Sci Technol 2020;177:103115. https://doi.org/10.1016/j.coldregions.2020.103115.

[18] Doroshkevich AG, Veksler IV, Klemd R, Khromova EA, Izbrodin IA. Trace-element composition of minerals and rocks in the Belaya Zima carbonatite complex (Russia): Implications for the mechanisms of magma evolution and carbonatite formation. Lithos 2017;284–285:91–108.

[19] Wang H, Wang Z, Wang J, Wang S, Wang H, Yin Y, et al. Effect of confining pressure on damage accumulation of rock under repeated blast loading. Int J Impact Engng 2021;156:103961. https://doi.org/10.1016/j.ijimpeng.2021.103961.

[20] Wasowski J, McSaveney MJ, Pisano L, Del Gaudio V, Li Y, Hu W. Recurrent rock avalanches progressively dismantle a mountain ridge in Beichuan County, Sichuan, most recently in the 2008 Wenchuan earthquake. Geomorphology 2021;374:107492. https://doi.org/10.1016/j.geomorph.2020.107492.

[21] Wang J, Chen G, Xiao Y, Li S, Chen Y, Qiao Z. Effect of structural planes on rockburst distribution: Case study of a deep tunnel in Southwest China. Engng Geol 2021;292:106250. https://doi.org/10.1016/j.enggeo.2021.106250.

[22] Ai D, Zhao Y, Wang Q, Li C. Experimental and numerical investigation of crack propagation and dynamic properties of rock in SHPB indirect tension test. Int J Impact Engng 2019;126:135–46.

[23] Kong X, Wang E, Li S, Lin H, Zhang Z, Ju Y. Dynamic mechanical characteristics and fracture mechanism of gas-bearing coal based on SHPB experiments. Theor Appl Fract Mech 2020;105:102395. https://doi.org/10.1016/j.tafmec.2019.102395.

[24] Fakhimi A, Azhdari P, Kimberley J. Physical and numerical evaluation of rock strength in Split Hopkinson Pressure Bar testing. Comput Geotech 2018;102:1–11.

[25] Gong F-Q, Si X-F, Li X-B, Wang S-Y. Dynamic triaxial compression tests on sandstone at high strain rates and low confining pressures with split Hopkinson pressure bar. Int J Rock Mech Min Sci 2019;113:211–9.

[26] Zwiessler R, Kenkmann T, Poelchau MH, Nau S, Hess S. On the use of a split Hopkinson pressure bar in structural geology: High strain rate deformation of Seeberger sandstone and Carrara marble under uniaxial compression. J Struct Geol 2017;97:225–36.

[27] Wen S, Zhang C, Chang Y, Hu P. Dynamic compression characteristics of layered rock mass of significant strength changes in adjacent layers. J Rock Mech Geotech Engng 2020;12(2):353–65.

[28] Mu L, Zhang Y. Cracking elements method with 6-node triangular element. Finite Elem Anal Des 2020;177:103421. https://doi.org/10.1016/j.finel.2020.103421.

[29] Zhang Y, Mang HA. Global cracking elements: A novel tool for Galerkin-based approaches simulating quasi-brittle fracture. Int J Numer Meth Engng 2020;121(11):2462–80.

[30] Zhang Y, Zhuang X. Cracking elements method for dynamic brittle fracture. Theor Appl Fract Mech 2019;102:1–9.

[31] Saadat M, Taheri A, Kawamura Y. Incorporating asperity strength into rock joint constitutive model for approximating asperity damage: An insight from DEM modelling. Engng Fract Mech 2021;248:107744. https://doi.org/10.1016/j.engfracmech.2021.107744.

[32] Xue Y, Zhou J, Liu C, Shadabfar M, Zhang J. Rock fragmentation induced by a TBM disc-cutter considering the effects of joints: A numerical simulation by DEM. Comput Geotech 2021;136:104230. https://doi.org/10.1016/j.compgeo.2021.104230.

[33] Hu W, Chen Z. Model-based simulation of the synergistic effects of blast and fragmentation on a concrete wall using the MPM. Int J Impact Engng 2006;32(12):2066–96.

[34] Diana V, Labuz JF, Biolzi L. Simulating fracture in rock using a micropolar peridynamic formulation. Engng Fract Mech 2020;230:106985. https://doi.org/10.1016/j.engfracmech.2020.106985.

[35] Han F, Lubineau G, Azdoud Y. Adaptive coupling between damage mechanics and peridynamics: A route for objective simulation of material degradation up to complete failure. J Mech Phys Solids 2016;94:453–72.

[36] Wang Y, Han F, Lubineau G. Strength-induced peridynamic modeling and simulation of fractures in brittle materials. Comput Methods Appl Mech Engng 2021;374:113558. https://doi.org/10.1016/j.cma.2020.113558.

[37] Mardalizad A, Saksala T, Manes A, Giglio M. Numerical modeling of the tool-rock penetration process using FEM coupled with SPH technique. J Petrol Sci Engng 2020;189:107008. https://doi.org/10.1016/j.petrol.2020.107008.

[38] Wang Y, Bui HH, Nguyen GD, Ranjith PG. A new SPH-based continuum framework with an embedded fracture process zone for modelling rock fracture. Int J Solids Struct 2019;159:40–57.

[39] Cruz F, Roehl D, Vargas EDA. An XFEM element to model intersections between hydraulic and natural fractures in porous rocks. Int J Rock Mech Min Sci 2018;112:385–97.
[40] Wang S, Li D, Mitri H, Li H. Numerical simulation of hydraulic fracture deflection influenced by slotted directional boreholes using XFEM with a modified rock fracture energy model. J Petrol Sci Engng 2020;193:107375. https://doi.org/10.1016/j.petrol.2020.107375.
[41] Zhang Y, Lackner R, Zeiml M, Mang HA. Strong discontinuity embedded approach with standard SOS formulation: element formulation, energy-based crack-tracking strategy, and validations. Comput Methods Appl Mech Engng 2015;287:335–66.
[42] Zhang Y, Gao Z, Li Y, Zhuang X. On the crack opening and energy dissipation in a continuum based disconnected crack model. Finite Elem Anal Des 2020;170:103333. https://doi.org/10.1016/j.finel.2019.103333.
[43] Zhang Y, Zhuang X. Cracking elements: A self-propagating strong discontinuity embedded approach for quasi-brittle fracture. Finite Elem Anal Des 2018;144:84–100.
[44] Ai W, Augarde CE. Thermoelastic fracture modelling in 2D by an adaptive cracking particle method without enrichment functions. Int J Mech Sci 2019;160:343–57.
[45] Kumar V, Ghosh A. Modeling of dynamic fracture based on the cracking particles method. Theor Appl Fract Mech 2015;75:22–31.
[46] Rabczuk T, Song J-H, Belytschko T. Simulations of instability in dynamic fracture by the cracking particles method. Engng Fract Mech 2009;76(6):730–41.
[47] Han F, Liu S, Lubineau G. A dynamic hybrid local/nonlocal continuum model for wave propagation. Comput Mech 2021;67(1):385–407.
[48] Han F, Lubineau G, Azdoud Y, Askari A. A morphing approach to couple state-based peridynamics with classical continuum mechanics. Comput Methods Appl Mech Engng 2016;301:336–58.
[49] Wu L, Huang D. Energy dissipation study in impact: From elastic and elastoplastic analysis in peridynamics. Int J Solids Struct 2022;234-235:111279. https://doi.org/10.1016/j.ijsolstr.2021.111279.
[50] Xu C, Yuan Y, Zhang Y, Xue Y. Peridynamic modeling of prefabricated beams post-cast with steelfiber reinforced high-strength concrete. Struct Concr 2021;22(1):445–56.
[51] Zhang Y, Yang X, Wang X, Zhuang X. A micropolar peridynamic model with non-uniform horizon for static damage of solids considering different nonlocal enhancements. Theor Appl Fract Mech 2021;113:102930. https://doi.org/10.1016/j.tafmec.2021.102930.
[52] Pan C, Li X, He L, Li J. Study on the effect of micro-geometric heterogeneity on mechanical properties of brittle rock using a grain-based discrete element method coupling with the cohesive zone model. Int J Rock Mech Min Sci 2021;140:104680. https://doi.org/10.1016/j.ijrmms.2021.104680.
[53] Wei X-D, Nguyen NHT, Bui HH, Zhao G-F. A modified cohesive damage-plasticity model for distinct lattice spring model on rock fracturing. Comput Geotech 2021;135:104152. https://doi.org/10.1016/j.compgeo.2021.104152.
[54] Nairn JA, Aimene YE. A re-evaluation of mixed-mode cohesive zone modeling based on strength concepts instead of traction laws. Engng Fract Mech 2021;248:107704. https://doi.org/10.1016/j.engfracmech.2021.107704.
[55] Jiang H, Meng D. 3D numerical modelling of rock fracture with a hybrid finite and cohesive element method. Engng Fract Mech 2018;199:280–93.
[56] Dahi Taleghani A, Gonzalez-Chavez M, Yu H, Asala H. Numerical simulation of hydraulic fracture propagation in naturally fractured formations using the cohesive zone model. J Petrol Sci Engng 2018;165:42–57.
[57] Meng Li, Tabiei A. An irreversible bilinear cohesive law considering the effects of strain rate and plastic strain and enabling reciprocating load. Engng Fract Mech 2021;252:107855. https://doi.org/10.1016/j.engfracmech.2021.107855.
[58] Zhou R, Chen H-M, Lu Y. Mesoscale modelling of concrete under high strain rate tension with a rate-dependent cohesive interface approach. Int J Impact Engng 2020;139:103500. https://doi.org/10.1016/j.ijimpeng.2020.103500.
[59] Zhao G, Xu J, Feng Y, Tang J, Chen Y, Xin S, et al. A rate-dependent cohesive zone model with the effects of interfacial viscoelasticity and progressive damage. Engng Fract Mech 2021;248:107695. https://doi.org/10.1016/j.engfracmech.2021.107695.
[60] Wang S, Li D, Li Z, Liu J, Gong S, Li G. A rate-dependent model and its user subroutine for cohesive element method to investigate propagation and branching behavior of dynamic brittle crack. Comput Geotech 2021;136:104233. https://doi.org/10.1016/j.compgeo.2021.104233.
[61] Lin Q, Li S, Feng C, Wang X. Cohesive fracture model of rocks based on multi-scale model and Lennard-Jones potential. Engng Fract Mech 2021;246:107627. https://doi.org/10.1016/j.engfracmech.2021.107627.
[62] Nasehzadeh A, Mohseni M, Azizi K. The effect of temperature on the Lennard-Jones (6–12) pair potential function. J Mol Struct (Thoechem) 2002;589–590:329–35.
[63] Dedkov GV, Kyasov AA. Dynamical van der Waals atom–surface interaction. Surf Sci 2011;605(11-12):1077–81.
[64] Dedkov GV, Kyasov AA. Dynamic van der Waals interaction of a moving atom with the walls of a flat slit. Tech Phys 2014;59(4):616–20.
[65] Ju Y, Liu P, Chen J, Yang Y, Ranjith PG. CDEM-based analysis of the 3D initiation and propagation of hydrofracturing cracks in heterogeneous glutenites. J Nat Gas Sci Engng 2016;35:614–23.
[66] Wang H, Bai C, Feng C, Xue K, Zhu X. An efficient CDEM-based method to calculate full-scale fragment field of warhead. Int J Impact Engng 2019;133:103331. https://doi.org/10.1016/j.ijimpeng.2019.103331.
[67] Wang X, Feng C, Zhu X, Zhang Li, Li S. A half-space based contact detection algorithm for complex blocks. Comput Geotech 2021;135:104168. https://doi.org/10.1016/j.compgeo.2021.104168.
[68] Zhu X, Feng C, Cheng P, Wang X, Li S. A novel three-dimensional hydraulic fracturing model based on continuum–discontinuum element method. Comput Methods Appl Mech Engng 2021;383:113887. https://doi.org/10.1016/j.cma.2021.113887.
[69] Feng C, Li S, Liu X, Zhang Y. A semi-spring and semi-edge combined contact model in CDEM and its application to analysis of Jiweishan landslide. J Rock Mech Geotech Engng 2014;6(1):26–35.
[70] Zhong H, Ma Z, Hu S, Fan X. Axial tensile tests for dynamic fracture characteristics of concrete-granite interface. J Vib Shock 2019;38:152–8.
[71] Yang R, Li W, Li Y, Fang S, Zhu Y. Comparative analysis on dynamic tensile mechanical properties of three kinds of rocks. J China Coal Soc 2020;45(9):3107–18.
[72] Wang F, Liu S, Cao L. Research on dynamic compressive behaviors of marble under high strain rates with split Hopkinson pressure bar. J Struct Geol 2020;138:104095. https://doi.org/10.1016/j.jsg.2020.104095.